This article has been accepted for publication in IEEE Sensors Journal. This is the author's version which has not been fully edited and content may change prior to final publication. Citation information: DOI 10.1109/JSEN.2025.3629803

3D Magnetic Field Camera with Sub-Second Temporal Resolution

F. Foerger, M. Boberg, N. Hackelberg, P. Heinisch, K. Ostaszewski, J. Faltinath, P. Suskin, F. Thieben, F. Mohn, P. Jürß, M. Möddel and T. Knopp

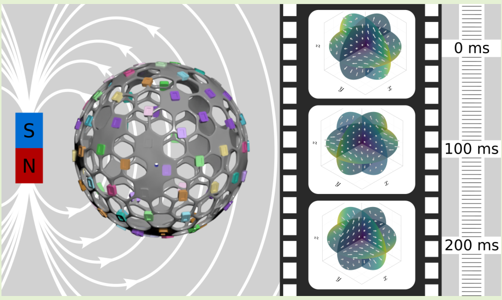

***Abstract*—Accurate and efficient volumetric magnetic field measurements are essential for a wide range of applications. Conventional methods are often limited in terms of measurement speed and applicability, or suffer from scaling problems at larger volumes. This work presents a proof-of-concept field camera designed to measure magnetic fields within a spherical volume at a frame rate of 10 Hz. The camera features an array of 3D Hall magnetometers positioned according to a spherical t-design, allowing simultaneous magnetic field data acquisition from the surface of the sphere. The approach enables the efficient representation of all three components of the magnetic field inside the sphere using a sixth-degree polynomial, significantly reducing measurement time compared to sequential methods. This work details the design, calibration, and measurement methods of the field camera. To evaluate its performance, we compare it to a sequential single-sensor measurement by examining a magnetic gradient field. The obtained measurement uncertainties of approx. 1% demonstrate the feasibility of the approach and its potential applicability to a variety of future applications.**

***Index Terms*—3D magnetic field mapping, Hall-effect devices, magnetic-field camera, magnetic-field sensors, magnetic sensor arrays, magnetometers**

I. INTRODUCTION

Magnetic fields play a crucial role in various areas, ranging from consumer products over industrial processes to scientific research and medical diagnostics. Their inherent ability to penetrate matter and interact with it in various ways enables a wide range of applications, including the transfer of forces and torques. The spatial distribution of magnetic fields is of high concern in most of these applications, as it directly influences the functionality and accuracy of the processes involved. One important area of magnetic fields in healthcare is tomographic imaging, which enabled the development of magnetic resonance imaging (MRI) [1] and magnetic particle imaging (MPI) [2]. Both imaging modalities use the superposition of different kinds of magnetic fields for signal generation and encoding. A detailed understanding of the magnetic field configuration is essential, as it directly underpins high-resolution imaging and precise diagnostics [3]–[5]. As a result, precise magnetic field measurements are frequently conducted and are essential for accurate imaging.

As shown in Figure 1a), a common approach to acquire such field data is to move a single 3D sensor through the volume of interest and sample the field sequentially at predefined positions. [6]. While this method provides reliable results, it is inherently time-consuming due to the necessity of precise and repeated sensor repositioning [7]. The associated measurement effort is exemplified by the empirical acquisition time indicated within the blue arrow for a 9 cm diameter spherical volume in the lower part of Figure 1. To overcome this challenge, previous research has focused on using the physical equations underlying the magnetic field to derive field models from comparatively few measurement points. When aiming to measure magnetic fields within a volume, one can exploit the fact that, in regions without current density, the magnetic field components satisfy the Laplace equation. This implies that each field component can be represented as a series expansion of spherical harmonics. By acquiring a limited set of surface measurements, as illustrated in Figure 1 b), the expansion coefficients can be uniquely determined, enabling the estimation of the entire magnetic field inside as a polynomial function. [8]–[12] For a spherical volume, by incorporating an efficient quadrature on the surface with points at spherical t-design positions [6], [13], fields can be

---

Submitted: August 2025, Funding: This work was supported in part by the German Research Foundation (DFG) under Grant KN 1108/2-2

The authors F. Foerger, M. Boberg, N. Hackelberg, J. Faltinath, P. Suskin, F. Thieben, F. Mohn, P. Jürß, M. Möddel and T. Knopp are with the Section for Biomedical Imaging, University Medical Center Hamburg-Eppendorf, Hamburg, Germany and with the Institute for Biomedical Imaging, Hamburg University of Technology, Hamburg, Germany (e-mail: fynn.foerger@tuhh.de)

The authors P. Heinisch and K. Ostaszewski are with Institut für angewandte numerische Wissenschaft, Braunschweig, Germany, the Institut für Geophysik und extraterrestrische Physik, Technische Universität Braunschweig, Braunschweig, Germany and the PhySens GmbH, Braunschweig, Germany

F. Foerger, N. Hackelberg, F. Thieben and T. Knopp are also with the Fraunhofer Research Institution for Individualized and Cell-Based Medical Engineering IMTE, Lübeck, Germany

This article has been accepted for publication in IEEE Sensors Journal. This is the author's version which has not been fully edited and
content may change prior to final publication. Citation information: DOI 10.1109/JSEN.2025.3629803

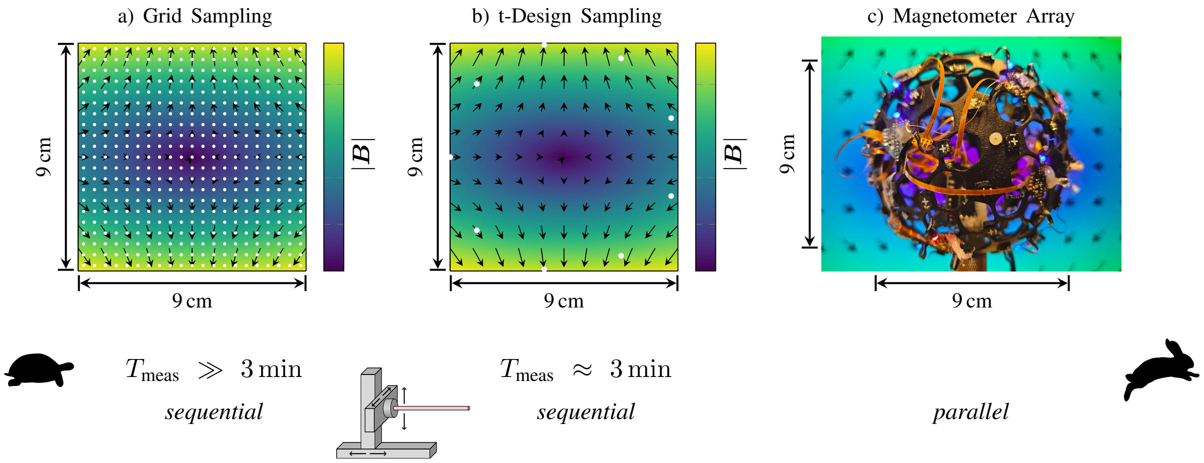

Fig. 1. Schematic representation of different magnetic field measurement methods using the illustrative example of a gradient field. The indicated measurement times T_{meas} refer to empirical values for a spherical measurement volume with a diameter of 9 cm. The left part illustrates a conventional approach using a single 3D Hall magnetometer that is sequentially moved to predefined grid points; white dots indicate the measurement positions. The middle part shows the subsequent magnetic field model from these discrete surface measurements. This sequential method typically requires several minutes. The right part depicts the approach presented in this work, in which a magnetometer array enables parallel field acquisition, allowing volumetric magnetic field measurements at rates of several Hertz.

calculated with small uncertainty using only a minimal number of measurement points [6].

Another way to achieve higher field acquisition rates is the use of multiple sensors at the same time. Schlageter et al. [14] and Vergne et al. [15], for example, used two-dimensional arrays of magnetometers to determine the position and orientation of a permanent magnet from the measured field in the respective plane, achieving refresh rates of 50 Hz and 2 Hz, respectively. Using a $7{\times}7$ array of Hall magnetometers in combination with an FPGA, Nicolas et al. [16] even reached sampling rates of up to 7 kHz. Sensor arrays are also used in particular in the field of research into micro-robots powered by magnetic fields to enable fast feedback for control, adaptive behavior, and dynamic trajectory planning. [17]–[21].

Dietrich et al. combined the field determination method of using surface measurements with spherical harmonics with an array of nuclear magnetic resonance (NMR) magnetometers in a spherical configuration. The result was a magnetic field camera that provides a three-dimensional map of the fields magnitude [4]. However, the NMR sensor requires a magnetic offset field and complex high frequency electronics for signal generation and acquisition, and does not measure the full field vector. With 16 field probes, the polynomial degree of the measurable field curves is also not sufficient for many applications. Another commercially available magnetic field measurement system uses NMR probes arranged in a semicircular geometry and requires multiple measurements at different angles to estimate the magnetic field [22]. As a result, detection times are far from the sub-second range, limiting its applicability.

In this work, our aim is to extend the approach proposed by Boberg et al. [6], which uses a t-design as a quadrature, by combining it with a spherical array of Hall magnetometers, as shown in Fig.1 c). With this setup, we present a proof-of-concept spherical magnetic field camera operating at an acquisition rate of 10 Hz. The system simultaneously acquires sensor data at the t-design positions, thereby reducing the measurement time significantly compared to the sequential single-sensor approach. With 86 three-axis magnetometers, the resulting model is a spherical harmonic expansion of all field components up to degree six, which can be evaluated at any point within the 9 cm diameter volume. Since the field camera is primarily intended for MPI magnetic field sequence planning, it must accommodate field strengths of several hundred mT [23]. Hall sensors are well suited for this field range while remaining cost-effective [24]. The high array sampling rate opens new possibilities for applications requiring fast field feedback. In addition, the method facilitates scaling to larger volumes or higher sensor counts due to its reduced hardware complexity.

The remainder of this paper is structured as follows: Section II presents the theory of the field estimation and the basis functions of the expansion. Section III introduces the characteristics of the field camera as well as the calibration procedure to compensate for sensor-specific systematic errors such as scaling, non-orthogonality, bias, and orientation. Section IV demonstrates the performance of the system using example measurements and evaluates the uncertainty of the field model. Finally, Sections V-VII conclude the paper and discuss possible future developments.

II. THEORY

This section outlines the theoretical basis and mathematical framework of the field model. It builds on prior knowledge of the physical relationships and uses measurements from the spherical magnetometer array to determine the coefficients of a

This article has been accepted for publication in IEEE Sensors Journal. This is the author's version which has not been fully edited and content may change prior to final publication. Citation information: DOI 10.1109/JSEN.2025.3629803

spherical harmonic expansion, enabling a compact representation of the field with high temporal resolution. A more detailed analysis can be found in Boberg et al. [6], which includes the complete derivation.

The fundamental equations governing electromagnetic phenomena are unified in Maxwell's equations. From these, in the quasi-static limit and in the absence of current densities, the magnetic flux density $\boldsymbol{B} : \mathbb{S}_R \to \mathbb{R}^3$ in the spherical volume under consideration $\mathbb{S}_R := \left\{\boldsymbol{a} \in \mathbb{R}^3 : \|\boldsymbol{a}\|_2 \leq R\right\}$, with radius $R \in \mathbb{R}_+$, is described by

$$\begin{aligned} \nabla \times \boldsymbol{B}\left(\boldsymbol{r}\right) &= \boldsymbol{0} \\ \nabla \cdot \boldsymbol{B}\left(\boldsymbol{r}\right) &= \boldsymbol{0}. \end{aligned} \tag{1}$$

It follows from these two equations that $\boldsymbol{B}$ satisfies Laplace's equation

$$\Delta B_i(\boldsymbol{r}) = 0, \quad i \in \{x, y, z\} \tag{2}$$

for each component. This fundamental property allows for the expansion of the magnetic flux density in terms of solid spherical harmonics

$$B_i(\boldsymbol{r}) = \sum_{l=0}^{\infty} \sum_{m=-l}^{l} \gamma_{l,m}^i Z_l^m(\boldsymbol{r}) \quad \forall \boldsymbol{r} \in \mathbb{B}_R \tag{3}$$

in the Ball $\mathbb{B}_R$ with the radius R, where $\gamma_{l,m}^i \in \mathbb{R}$ are the expansion coefficients and $Z_l^m(\boldsymbol{r})$ the solid spherical harmonic functions with

$$\begin{aligned} &Z_l^m : \mathbb{R}^3 \to \mathbb{R}, \\ &(r, \vartheta, \varphi) \mapsto K_l^{|m|} r^l P_l^{|m|}\left(\cos\left(\vartheta\right)\right) \begin{cases} \sqrt{2}\cos\left(m\varphi\right) & m > 0 \\ \sqrt{2}\sin\left(|m|\varphi\right) & m < 0 \\ 1 & m = 0 \end{cases}. \end{aligned} \tag{4}$$

Here, we have $K_l^m = \sqrt{\frac{(l-m)!}{(l+m)!}}$, and the associated Legendre polynomials P_l^m. The coefficients $\gamma_{l,m}^i$ can be calculated by applying the Dirichlet boundary condition

$$\gamma_{l,m}^i = \frac{2l+1}{R^l 4\pi} \int_{\mathbb{S}_R} B_i(\boldsymbol{r}) Z_l^m\left(\frac{\boldsymbol{r}}{R}\right) \, d\boldsymbol{r}. \tag{5}$$

In reality, the integral in (5) is solved by sampling the surface of the sphere at discrete points. In our case we use a quadrature, that features spherical t-design positions $\{\boldsymbol{r}_1, \ldots, \boldsymbol{r}_N\} \subseteq \partial\mathbb{S}_R$ as sampling points of the integral:

$$\gamma_{l,m}^i = \frac{2l+1}{R^l N} \sum_{k=1}^{N} B_i(\boldsymbol{r}_k) Z_l^m\left(\frac{\boldsymbol{r}_k}{R}\right) \tag{6}$$

Consequently, by selecting the t-design with the associated number of sampling nodes N, the expansion in (3) can be specified up to degree $\lfloor \frac{t}{2} \rfloor$:

$$B_i(\boldsymbol{r}) \approx \sum_{l=0}^{\lfloor \frac{t}{2} \rfloor} \sum_{m=-l}^{l} \gamma_{l,m}^i Z_l^m(\boldsymbol{r}) \quad \forall \boldsymbol{r} \in \mathbb{B}_R. \tag{7}$$

This field determination method is particularly robust because it holds that the approximation in (7) is exact if the field under consideration has a polynomial degree of at most $\lfloor \frac{t}{2} \rfloor$. Furthermore, each coefficient $\gamma_{l,m}^i$ is determined from all measured values on the surface, and all measurements contribute equally due to the uniform quadrature weights of the t-design. As a result, individual sensor uncertainties are naturally averaged out, and no single measurement disproportionately influences the field estimation [25].

Besides the spherical t-design, there are several other types of quadrature that can be considered, most notably the class of Gaussian quadratures [26]. For example, the combination of the trapezoidal rule and the Gauss-Legendre quadrature can provide an exact approximation for polynomials of the same degree as the t-design, but with a higher number of nodes [6], [26]. In addition, such Gaussian quadratures are limited by the physical size of the sensors, as nodes accumulate near the poles.

III. METHODS

The theory described in the last section is now applied to a measuring device for determining magnetic fields in a spherical volume. For this purpose, a magnetometer array consisting of Hall magnetometers is considered in which the field is measured simultaneously at positions defined by a spherical t-design.

A. Design Considerations

The field camera presented in this work is intended for magnetic field characterization in the context of MPI, particularly for field sequence planning in a custom-built MPI field generator [27]. In principle, the field estimation method described in Section II is flexible and can be applied to a wide range of magnetic field scenarios — including different spatial complexities, field strengths, and volumes. Depending on the intended application, the sphere size as well as the number and type of sensors can be adapted, in particular with respect to resolution and dynamic range.

In our specific application, several design requirements and constraints shaped the selection of key parameters of the field camera:

- Volume size: The field generator in which the field camera is intended to operate includes soft-magnetic pole pieces and features a coil separation of approximately 10 cm. It was therefore designed with a diameter of 9 cm to ensure sufficient clearance while still occupying a large portion of the field volume for accurate measurements.
- Number of sensors: The fields generated in such systems are highly non-linear. From previous experiments and simulation studies, we found that polynomial expansions of degree lower than 6 are not sufficient to capture the spatial complexity. A sixth-degree expansion requires a minimum of 86 sensors placed at t-design positions with $t = 12$ to ensure an accurate field model.
- Field strength range: In the target application, we expect magnetic field magnitudes up to 200 mT at the boundary of the spherical volume. The chosen Hall magnetometers offer a dynamic range of ±266 mT and are thus well suited for this use case.

- Sampling frequency: A high temporal resolution is always advantageous. While the hardware supports sampling rates of up to 10 kHz, we chose to internally average the raw data to reduce transfer bandwidth and improve signal quality. The effective rate of 10 Hz is sufficient for measuring MPI field sequences for the time being.

B. Field Camera Hardware

This section outlines how the requirements have been translated into the hardware implementation of the field camera. The inbuilt sensor array consists of 86 independent Hall magnetometers (Texas Instruments TMAG5273) arranged on the surface of a 3D printed sphere as shown in Fig. 2 with a radius of $45\,\mathrm{mm}$ made of polyamide. To conform to the spherical geometry, the individual sensors are mounted on submodules made of flexible printed circuit boards with a polyimide film substrate (see Fig. 2 - right panel). These also serves as electrical connection between the sensors and the centrally-mounted microcontroller mainboard. Each of these submodules is equipped with between four and five magnetometers to get up to the total number of 86, an intelligent serial-based multiplexing system to be able to control each sensor individually and a software controlled LED for submodule identification and testing. Power to the magnetometers is only applied during read-out to prevent interference. An appropriate delay was introduced in firmware and lab-tested to allow for the internal sensor hardware to start and the measurements to settle. For internal communications the industry standard "Inter-Integrated Circuit" (I²C) bus is used. The positions of the individual sensors were chosen based on a t-design with $t = 12$ and the magnetometer local y-axis aligned longitudinally and the local z-axis aligned to the position dependent surface normal. To reduce the possibility of interference, the power supply and filtering, data processing, and communications are located on a separate centrally-mounted main circuit board in the center of the sphere. A shielded, non-magnetic USB cable is used for the connection. The magnetometers provide internal temperature compensation. In addition, a temperature sensor is mounted at the center of the sphere to monitor the temperature and to indicate when the internal temperature compensation may no longer be sufficient to correct the sensor readings. Each component of the field camera was chosen individually to exclude any magnetic material. All upstream communications are handled via a 12 Mbps Full-Speed USB interface to further reduce high-frequency electromagnetic interference. The magnetometers have a total range of ±266 mT with a bit resolution of 8.12 µT. Three magnetometers are sampled at the same time spread out across the sphere to avoid interference. To achieve a near simultaneous sampling at an effective data rate of 10 Hz the individual sensors are being oversampled at a rate of 250 Hz and internally averaged. This reduces sensor noise while also conserving transfer bandwidth and computational requirements on the host system. According to the sensors data sheet, sampling rates up to 10 kHz can be achieved [28].

C. Calibration Method

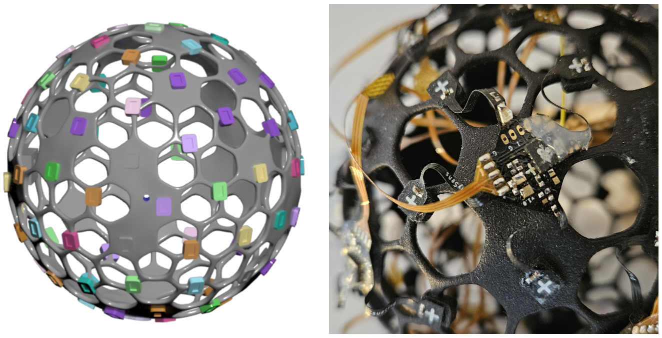

Fig. 2. Left: 3D rendering of the CAD model of the field camera. The colored rectangular structures provide mechanical support for the individual magnetometers and ensure correct alignment. Hexagonal cutouts allow for easy routing of the flexible printed circuit boards used to connect the magnetometers while still providing the necessary mechanical stiffness. Right: Close up of a flexible printed circuit board with attached sensors.

Hall magnetometer, by their nature, are sensitive to various external and internal factors that can affect their readings, hence a careful calibration is important, and the existing literature contains a variety of methods for achieving this [24]. For the inbuilt Hall magnetometer array, one additional challenge is the uncertainty regarding the exact position and orientation of each sensor within the array. Without a careful calibration, the collected data can be misinterpreted, leading to significant errors of the field representation. First, we describe how to transfer the measured values of the individual sensors into a shared coordinate system. Then we will discuss the calibration of the exact sensor position on the sphere, which we need in order to calculate the coefficients in (6).

1) Local Sensor Calibration:

As it can be seen in Fig. 3 a), each sensor in the array possesses its own local coordinate system in which it outputs its field values $\boldsymbol{b}^n$, where the index n denotes the sensor number. In the first part of the calibration, the values $\boldsymbol{b}^n$ from the local coordinate systems have to be transformed into a global coordinate system, resulting in values denoted by $\boldsymbol{B}^n$ illustrated in Fig. 3 b). Since the sensor operates within the specified linear range, a linear calibration model can be applied, expressed as

$$\boldsymbol{B}^n = \boldsymbol{R}^n \boldsymbol{b}^n + \boldsymbol{O}^n. \tag{8}$$

Here, $\boldsymbol{R}^n \in \mathbb{R}^{3\times 3}$ denotes the individual matrix of the n-th sensor for scaling, skew, and rotation and $\boldsymbol{O}^n \in \mathbb{R}^3$ represents the offset correction.

To determine both, the rotation matrix and the offset correction, linearly independent homogeneous magnetic fields with known strength and direction in the global coordinate system are applied to the entire device. To obtain a unique solution in this calibration model, $J \geq 4$ different calibration fields spanning $\mathbb{R}^3$ must be set, denoted by $\tilde{\boldsymbol{B}}_j \in \mathbb{R}^3$, where j is the index of the respective field set. $\boldsymbol{b}_j^n$ are the corresponding measured values of the n-th sensor when the j-th field is applied. To determine $\boldsymbol{R}^n$ and $\boldsymbol{O}^n$, the optimization problem

$$\underset{\boldsymbol{R}^n, \boldsymbol{O}^n}{\arg\min} \sum_{j=1}^{J} \left\| \tilde{\boldsymbol{B}}_j - \begin{pmatrix} \boldsymbol{R}^n & \boldsymbol{O}^n \end{pmatrix} \begin{pmatrix} \boldsymbol{b}_j^n \\ 1 \end{pmatrix} \right\|_2^2 \tag{9}$$

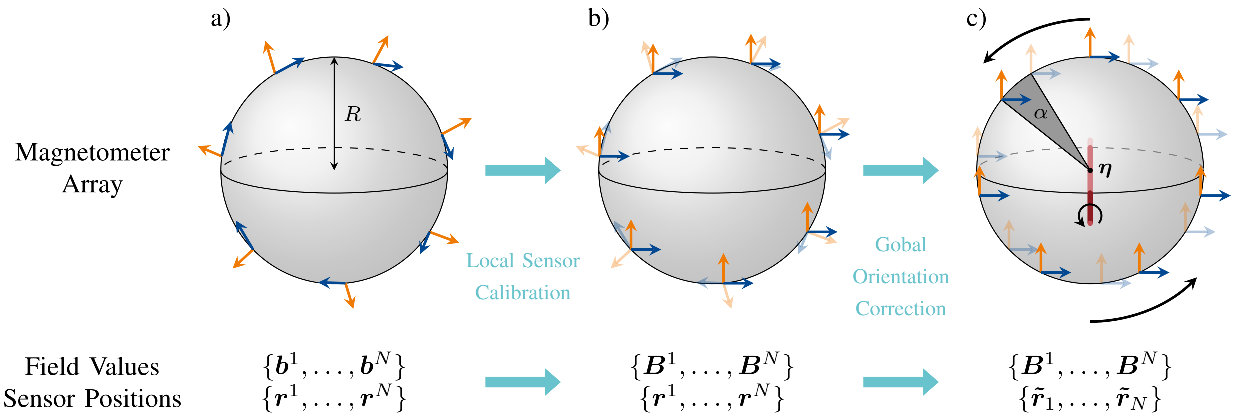

Fig. 3. Calibration procedure for the field camera. As shown in a), each Hall magnetometer at $\{\boldsymbol{r}^1,\dots,\boldsymbol{r}^N\}$ outputs its value in a local coordinate system $\{\boldsymbol{b}^1,\dots,\boldsymbol{b}^N\}$ that may not be orthogonal. From a) to b), all local coordinates systems must be transformed into a global coordinate system obtaining $\{\boldsymbol{B}^1,\dots,\boldsymbol{B}^N\}$ to solve the surface integral for calculation of the expansion coefficients. In a second step from b) to c), the corrected t-design positions $\{\tilde{\boldsymbol{r}}_1,\dots,\tilde{\boldsymbol{r}}_N\}$ in the coordinate system of the calibration fields are found by applying a global rotation around the axis $\boldsymbol{\eta}$ by the angle α

has to be solved.

In our case, this is done by reformulating the residuum in (9). Since the second term of it is linear in $\begin{pmatrix}\boldsymbol{R}^n & \boldsymbol{O}^n\end{pmatrix}$, a matrix $\mathfrak{B}_{b_j^n} \in \mathbb{R}^{3\times 12}$ exists such that

$$\begin{pmatrix}\boldsymbol{R}^n & \boldsymbol{O}^n\end{pmatrix}\begin{pmatrix}\boldsymbol{b}_j^n \\ 1\end{pmatrix} = \mathfrak{B}_{b_j^n}\begin{pmatrix}\mathrm{vec}\left(\boldsymbol{R}^n\right) \\ \boldsymbol{O}^n\end{pmatrix} \tag{10}$$

By concatenating all $\mathfrak{B}_{b_j^n}$ vertically one can express (9) as

$$\underset{\boldsymbol{R}^n,\boldsymbol{O}^n}{\arg\min}\left\|\begin{pmatrix}\tilde{\boldsymbol{B}}_1 \\ \vdots \\ \tilde{\boldsymbol{B}}_j\end{pmatrix} - \begin{pmatrix}\mathfrak{B}_{b_1^n} \\ \vdots \\ \mathfrak{B}_{b_j^n}\end{pmatrix}\begin{pmatrix}\mathrm{vec}\left(\boldsymbol{R}^n\right) \\ \boldsymbol{O}^n\end{pmatrix}\right\|_2^2 \tag{11}$$

which is solved by a pivoted QR factorization.

2) Global Orientation Correction: The coordinate system of $\tilde{\boldsymbol{B}}_j$ now determines the new coordinate system of the field camera. However, we only know the positions of the sensors $\{\boldsymbol{r}_1,\dots,\boldsymbol{r}_N\}$ in the coordinate system of the CAD model of the 3D printed sensor mount. In order to express the field using the series expansion, the next step is to specify the sensor positions in the calibration field coordinate system, resulting in corrected t-design positions $\{\tilde{\boldsymbol{r}}_1,\dots,\tilde{\boldsymbol{r}}_N\}$. Assuming that the calibration fields coordinate system is Cartesian, the correction of the t-design positions can be represented by a global rotation matrix $\boldsymbol{M} \in \mathrm{SO}(3)$ that rotates all positions such that

$$\tilde{\boldsymbol{r}}_n = \boldsymbol{M}\boldsymbol{r}_n,\ n \in \{1,...,N\}. \tag{12}$$

Even if the sphere coordinate system is carefully aligned with the calibration fields coordinate system, a slight sag in the mounting can cause the sensors to rotate out of their expected positions.

For the estimation of $\boldsymbol{M}$, we use a measurement-based approach, combining the calibration measurement data with prior knowledge about the mounting of the sensors on the sphere's surface. In the case of our magnetometer array, the z-axes of the sensors are assumed to be perpendicular to the sphere's surface and oriented outward. This allows for an initial estimation of the sensor positions based on the orientation of their coordinate systems, which were previously derived from measurements with the calibration fields. The z-axis of a sensor in the coordinate system of the applied calibration fields points in the same direction as $\boldsymbol{R}^n_{:,z}$, which denotes the z column of $\boldsymbol{R}^n$. We now assign to each sensor an estimated position

$$\hat{\boldsymbol{r}}_n = R\frac{\boldsymbol{R}^n_{:,z}}{\left\|\boldsymbol{R}^n_{:,z}\right\|_2}. \tag{13}$$

Due to measurement inaccuracies or sensor misalignment the set of positions $\{\hat{\boldsymbol{r}}_1,\dots,\hat{\boldsymbol{r}}_N\}$ are in general no spherical t-design positions.

We now search for the rotation matrix $\boldsymbol{M}$ that optimally aligns the t-design positions from the CAD model, $\{\boldsymbol{r}_1,\dots,\boldsymbol{r}_N\}$ with the estimated sensor positions, $\{\hat{\boldsymbol{r}}_1,\dots,\hat{\boldsymbol{r}}_N\}$. Specifically, we aim to minimize the sum of squared spherical distances between these two sets of positions on the sphere $\mathbb{S}_R$ with radius R

$$\underset{\boldsymbol{M}\in\mathrm{SO}(3)}{\arg\min}\sum_{n=1}^{N} d_{\mathbb{S}_R}\left(\boldsymbol{M}\boldsymbol{r}_n, \hat{\boldsymbol{r}}_n\right)^2, \tag{14}$$

where $d_{\mathbb{S}_R} : \mathbb{S}_R \times \mathbb{S}_R \to \mathbb{R}$ is the spherical distance.

To solve the optimization problem, we parameterize $\boldsymbol{M}$ using a rotation angle $\alpha \in \mathbb{R}$ and a rotation axis $\boldsymbol{\eta} \in \mathbb{R}^3$ and employ the Manifolds.jl [29] package to accurately compute the spherical distances. The optimization is then performed by gradient descent using Manopt.jl [30], which provides a framework for optimization on manifolds as well as a Library of optimization algorithms in Julia [31]. As it can be seen in Fig. 3 c), the calculated rotation matrix $\boldsymbol{M}$ can then be applied to the sensor positions.

D. Calibration Setup

For calibration, the sphere is placed in a homogeneous magnetic field in $J = 6$ different orientations. It is generated

This article has been accepted for publication in IEEE Sensors Journal. This is the author's version which has not been fully edited and content may change prior to final publication. Citation information: DOI 10.1109/JSEN.2025.3629803

by a solenoid[1] with an inner diameter of $30\,\mathrm{cm}$. All calibration measurements were performed at a field strength of $20.08\,\mathrm{mT}$ (including the Earth's magnetic field, measured with a Hall magnetometer, model 460, Lake Shore, Westerville, USA), with each measurement lasting three minutes. A total of 1800 individual measurements were obtained, and their mean value was utilized to ascertain all parameters of the calibration model. The relative homogeneity of the solenoid field, defined as the change in the field norm, in the spherical region is approximately $1.1 \cdot 10^{-3}$. Inside the volume of the Hall magnetometer, a field component perpendicular to the coil axis is generated that is approximately $1.15\,\%$ of the nominal flux density. We consider the values to be sufficiently small to assume the field as homogeneous. Since the solenoid can only apply the field in one direction, the sphere is placed in the field in different orientations using a cubic cage mount. The right-angled structure of the mount makes it possible to record the calibration fields along the three orthogonal axes of the sphere.

E. Uncertainty Propagation

To assess the robustness of the estimated field model, we performed an uncertainty propagation analysis based on sensor-specific input uncertainties. The analysis includes sensor noise and drift, spatial inhomogeneities and determination uncertainties in the calibration field, as well as positioning and orientation errors of the individual sensors. A Monte-Carlo approach was used to estimate the resulting spatially dependent uncertainty in the field. Details of the method and a comprehensive discussion of the results are presented in a separate work [32].

F. Experimental Setup

The field measurement method using a t-design quadrature to discretize the field on the surface of the sphere to infer the field is already well established [6]. We therefore compare the data from the field camera with a second measurement, also using a spherical t-design with $t = 12$ and $R = 9\,\mathrm{cm}$, and a spherical harmonic expansion, but recorded sequentially. The data were obtained using a single 3D Hall magnetometer (Model 460, Lake Shore, Westerville, USA) mounted on a robot that moves the sensor to t-design positions. For both measurement methods, a magnetic gradient field with a characteristic field-free point (FFP) and gradient strengths of $0.22\,\mathrm{T\,m^{-1}}$ in the y-direction and $0.11\,\mathrm{T\,m^{-1}}$ in x- and z-directions was analyzed. This field is generated by two identical coils mounted on a common soft-iron yoke. Details on the design and calibration of the setup, including verification of the gradient strengths, can be found in [33]. The field is particularly well represented by a sixth-degree polynomial. This ensures that truncation errors are minimal and that deviations likely stem from the proposed calibration method, which we aim to investigate.

For a meaningful comparison, it is important to ensure that we measure the same volume and in the same orientation. By aligning the FFPs to the center of each measurement volume it is guaranteed that both approaches capture the same region. To achieve proper orientation, the field camera is initially rotated as precisely as possible to align its axes with those of the single sensor measurement. Any remaining misorientation is corrected by applying an additional optimization in a post-processing step by using a simplex algorithm, which rotates the field to best match that of the single sensor measurement. The measurement setup can be seen in Fig. 4 on the left. Additionally, the sphere's radius is included in the optimization to compensate for minor discrepancies in size due to possible inaccuracies in the 3D printing process. To obtain statistical values for the deviation of the two field measurement methods, the field within the sphere is sampled Cartesian with a grid spacing of $0.5\,\mathrm{mm}$.

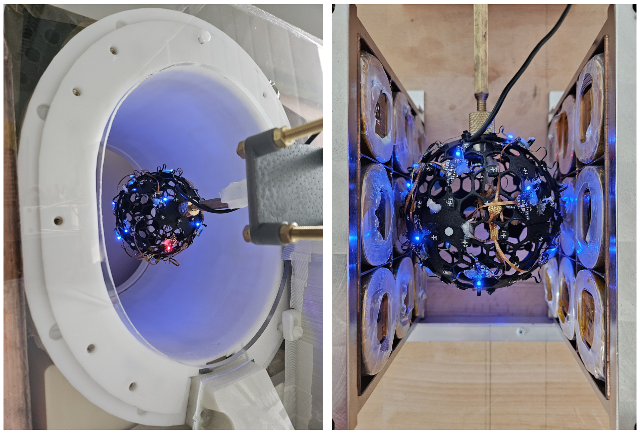

Fig. 4. Left: Measurement setup for measuring the gradient field of the magnetic particle imaging system on a human head size with the field camera. The camera is attached to a robot that can move the sphere through the imaging area in the bore of the system. The coils under the cover generate a field with a field-free point that is located in the center of the sphere after adjustment [33]. Right: Measurement setup for the FFP trajectory. The field camera is placed inside an 18-coil magnetic field generator consisting of two 3×3 coil arrays. Sinusoidal coil currents with different phases produce a field-free point that moves on an ellipsoidal trajectory inside the sphere [27].

In a second experiment, we qualitatively demonstrate the ability of the field camera to capture dynamic field sequences at video rates. For this purpose, a soft-iron coil array [27] was used to generate a time-dependent gradient field that produced a dynamic FFP. The array consists of 18 coils, arranged in two planar 3×3 sub-arrays on opposite sides of the field of view. Sinusoidal currents with different amplitudes and phases were applied to the individual coils, resulting in a combined magnetic field that drives the FFP along a continuous oval trajectory with varying speed inside the spherical measurement volume. The field was activated for about $5\,\mathrm{s}$, during which the FFP performed one full oscillation. The trajectory of the FFP was recorded live at $10\,\mathrm{Hz}$ using the field camera. The measured data were transferred serially via USB to a computer, where the spherical harmonic field model was reconstructed from the field values at the t-design positions. The right part of Fig. 4 shows a photo of the measurement setup from above.

IV. RESULTS

---

[1] Calibrating coil manufactured by Sekels, location: Ober-Mörlen, Germany

This article has been accepted for publication in IEEE Sensors Journal. This is the author's version which has not been fully edited and
content may change prior to final publication. Citation information: DOI 10.1109/JSEN.2025.3629803

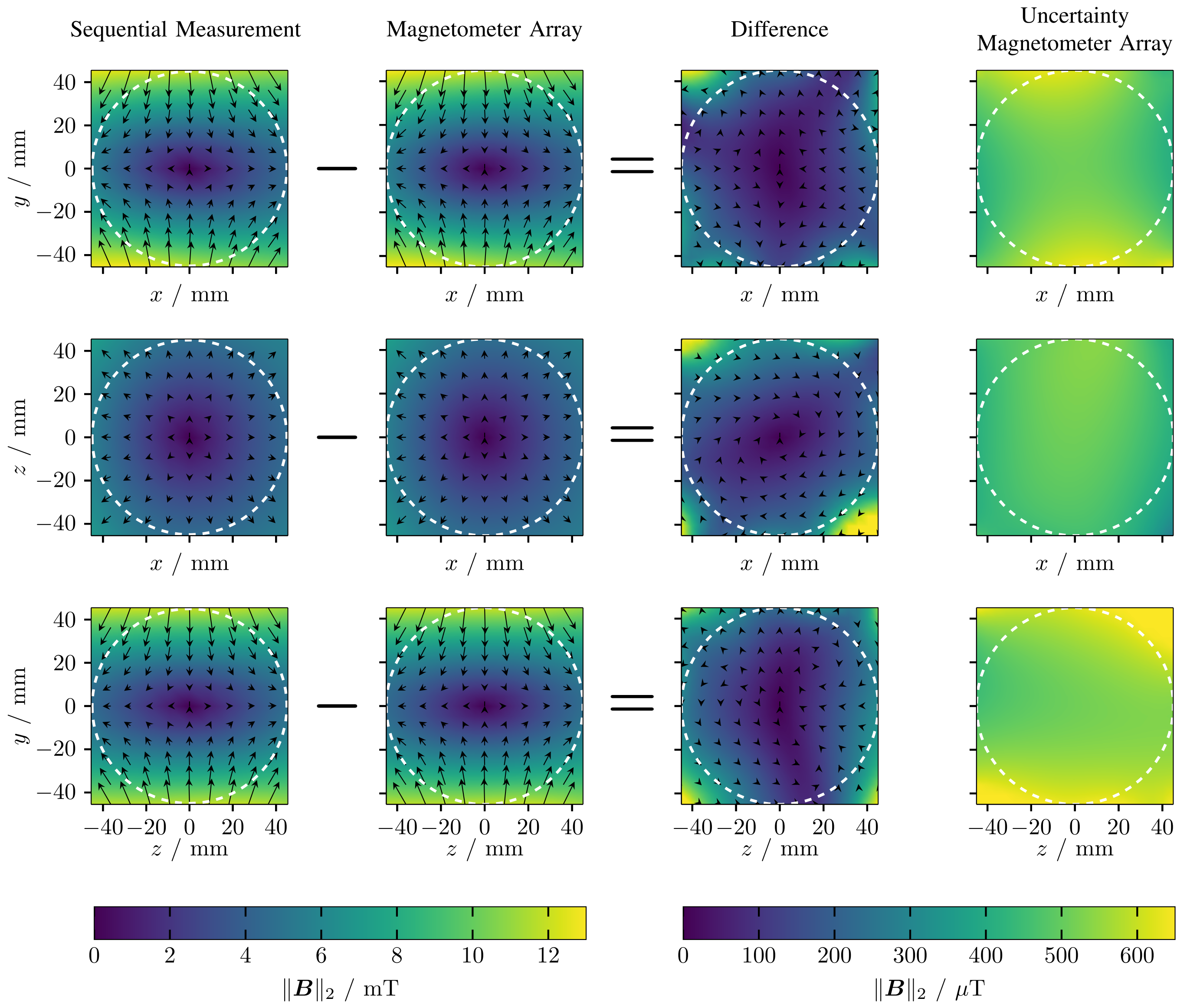

Fig. 5. Comparison of field measurements from the single sensor approach and the field camera across three orthogonal planes. The examined field is a gradient field with a field-free point at the center and a gradient strength of 0.22 T m^{-1} in y-direction and 0.11 T m^{-1} in x- and z-direction. The first column displays the sequential single sensor data, the second column the field camera data, and the third column the magnitude and direction of the difference vector between the two measurements. The fourth column shows the propagated uncertainty of the field norm on the planes for the field camera. Only inside the sphere's boundary (white circle), the fields series expansion is valid. Values outside are to be ignored.

We first consider the results for the measurement of the static gradient field. Both, the single-sensor and the field camera yield very similar magnetic field measurements, but with very different scan times. While sequential measurement with a single sensor and a robot takes about 3 min, the field camera provides equivalent data in only 100 ms.

The optimization in the post-processing step to align the two field measurements with each other resulted in a tilt angle of 1.8°. The optimized radius of the sphere is 45.41 mm. After correcting for the misalignment and scaling of the radius, the average norm of the difference field of the two fields within the sphere is (154 ± 66) µT (mean ± standard deviation), while the maximum is 403 µT. In relation to the maximum magnitude of the field within the sphere of 12.0 mT, this results in an average deviation of about 1% and a maximum deviation of about 4%. A plot of the field obtained by the two measurement methods as a plot of the difference field on the cross-sectional planes is shown in Fig. 5. A direct comparison of the two measurement methods is presented in Fig. 7. The figure shows the measured absolute field values (left column) and the absolute value of the difference field (right column) along the coordinate axes from Fig. 5. For both plots it can be seen that the largest absolute deviations are observed at the edge of the sphere. Note that the approximation of the field by a spherical harmonic expansion does not provide information about the field outside this sphere [6], as indicated by the white dashed line.

The uncertainty propagation was performed separately for

This article has been accepted for publication in IEEE Sensors Journal. This is the author's version which has not been fully edited and
content may change prior to final publication. Citation information: DOI 10.1109/JSEN.2025.3629803

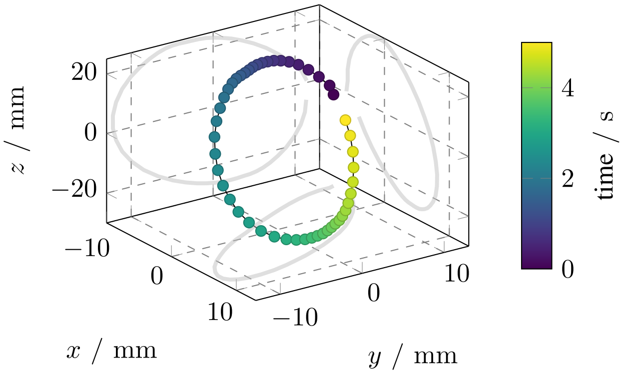

Fig. 6. Measured positions of the field-free point (FFP) during a periodic magnetic field sequence of 5 s duration, recorded at 10 Hz. Instead of plotting the full volumetric field, only the time-dependent FFP positions are shown as circular markers. The color scale indicates the chronological order of the trajectory for enhanced visualization. Gray curves show the projections onto the coordinate planes.

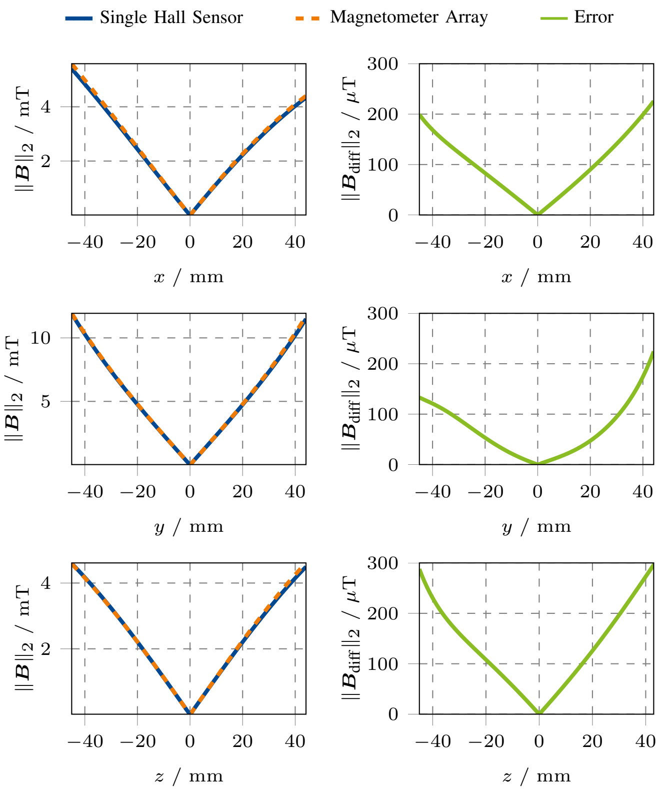

Fig. 7. Comparison of field measurements using the single-sensor approach and the field camera along the three coordinate axes. The left diagrams depict the absolute field values for both methods, while the right diagrams illustrate the magnitude of the difference field between the two measurements.

each magnetic field component. The resulting average uncertainties within the sphere were estimated as 200 μT for B_x, 270 μT for B_y, and 210 μT for B_z. This corresponds to a mean uncertainty of 400 μT in the magnitude of the field. A breakdown of the individual contributions reveals that the dominant source of uncertainty is the spatial inhomogeneity of the calibration field, contributing 310 μT. Positional and orientational uncertainties of the sensors follow with 220 μT, while sensor-specific effects such as noise and drift account for the smallest contribution with 140 μT. The right column of Fig. 5 shows the spatially dependent propagated uncertainty of the magnetic field norm in the respective planes [32].

Fig. 6 shows the recorded trajectory of an FFP moving inside the spherical volume. Within 5 s, 50 magnetic field shots were taken. The trajectory is oval in shape and the speed of the FFP varies according to its position, as can be seen from the different distances between the recorded points along the trajectory.

V. DISCUSSION

The results demonstrate that the calculated model accurately reproduces the field obtained from the sequential measurement, which has been validated as a reliable representation of the real field in prior work. Measurement uncertainty depends on both the complexity of the spatial profile of the magnetic fields being analyzed and the calibration process. In particular, fields that can be well approximated by a polynomial of degree 6 can be accurately estimated. Since the analyzed field fulfills this requirement, we can focus here on errors originating from other sources of uncertainty.

The uncertainty analysis presented in [32] identifies inhomogeneities in the calibration fields $\tilde{\boldsymbol{B}}_j$ as the dominant source of uncertainty. This highlights the importance of using highly homogeneous calibration fields and knowing their absolute amplitudes with low uncertainty in order to minimize systematic uncertainties for the field measurements.

Errors in sensor positioning and orientation also contribute to the overall uncertainty, albeit to a lesser extent. Although the field estimation method averages out local deviations, it is still essential to carefully place the sensors on the spherical surface to reduce their impact.

A further limiting factor is the susceptibility of Hall magnetometers to temporal drifts, which can be caused by sensor aging. These effects can be either correlated or uncorrelated across sensors. In the correlated case, systematic deviations can arise, which are not mitigated by averaging. Uncorrelated uncertainties, in contrast, are more likely to average out during the coefficient estimation process. Nevertheless, periodic recalibration of the field camera is required to maintain long-term precision.

Additional uncertainty stems from imperfections in the 3D-printed sensor holder, which may deviate from a perfect sphere due to manufacturing tolerances or thermal deformation over time. For example, in a field gradient of 0.2 T m^{-1}, a radial displacement of only 1 mm can lead to a field deviation of 200 μT. Systematic deviations from the intended geometry can introduce distortions in the measured field gradients that cannot be compensated for by simply adjusting the sphere radius during optimization.

Considering all these factors, the observed average deviation of 154 μT between two independent measurement methods aligns well with the propagated uncertainties and supports the validity of the presented approach. We acknowledge that testing only a single gradient field does not guarantee performance across all possible field configurations. However, the main error sources relevant to our setup, such as calibration inaccuracies or deformations of the 3D-printed holder, would also manifest themselves in the static gradient field measurement used for validation. The agreement observed between the sequential and field camera measurements therefore provides confidence that these errors do not compromise usability.

Mean uncertainties of about 400 µT determined by the uncertainty propagation are already sufficient for the intended use case of MPI sequence design and planning, where field strengths lie in the several mT range and spatial tolerances are on the millimeter scale. For example, such an uncertainty corresponds to a shift of the field of view in the MPI scanner on the order of 1 to 2 mm, which is smaller than the positioning accuracy with which a human head can realistically be placed inside the scanner. However, for applications that require significantly higher absolute field accuracy, the dominant sources of error can be further reduced.

Comparing the measurement time of the sequential and parallel methods for a spherical volume with a diameter of 9 cm, the parallel measurement results in a speedup by a factor of about 1800. With this frame rate, a wide range of dynamic field sequences can already be investigated. As an example, we recorded the trajectory of a moving FFP in a field generator. The observed oval trajectory and varying speed are expected, since the circular motion was only approximated by the coil currents and not realized through a precisely controlled field sequence. The strong field inhomogeneity and varying gradient strengths within the volume further prevent a uniform FFP movement.

It should be noted that the field camera averages the measured data over 100 ms and transmits the averaged values as a single frame. The resulting reconstructions therefore represent mean fields over this time window. The latency from data acquisition to visualization cannot be precisely specified at this stage, but in our current prototype it is dominated by unoptimized plotting algorithms rather than by the field reconstruction itself.

VI. CONCLUSION

The method of measuring magnetic fields at spherical t-design positions and modeling the field within the sphere's volume using a spherical harmonic expansion was successfully applied to a magnetometer array. This constitutes a proof-of-concept, demonstrating that the approach can be successfully implemented in hardware. The presented calibration procedures enabled monitoring of a magnetic field that can be well represented by a polynomial of degree six, with a temporal resolution of 10 Hz and an uncertainty in the 100 µT range. This capability opens up entirely new application scenarios where the spatio-temporal distribution of magnetic fields is of interest.

The field camera is particularly relevant for MPI, where both static and dynamic field information are crucial. For instance, the ability to track an FFP trajectory at video rates enables direct monitoring of time-varying selection fields. This knowledge directly impacts the calculation of the imaging field of view, the achievable resolution [5], and the performance of model-based reconstructions [34], [35]. Applications such as the planning and characterization of multi-patch sequences [23] especially benefit from fast volumetric measurements, since the field evolution under the combined influence of coil currents and eddy currents can be mapped directly. Achieving this with sequential single-sensor measurements would be prohibitively time-consuming, as it would require many time-triggered measurements during each sequence.

Beyond MPI, the field camera is also well suited for other applications where repeated volumetric field mapping is required. Examples include shimming in MRI systems, where field inhomogeneities must be iteratively assessed and corrected [36]; calibration of magnetic manipulation platforms for microrobotics or drug delivery [37]; magnetic tracking systems that rely on accurate field maps to improve localization accuracy [38]–[41]; haptic interfaces that use shaped magnetic fields to provide tactile feedback [42]; and the volumetric field mapping of superconducting magnets in particle accelerators, where harmonic control and precise field characterization are essential [43]. In general, experimental mapping becomes particularly important when magnetic fields are influenced by materials with poorly characterized magnetic properties, which are difficult to capture reliably in simulations. Finally, the method inherently offers good scalability, making it adaptable to larger volumes or higher sensor counts.

VII. OUTLOOK

Future work will focus on refining the calibration process by performing it in more homogeneous and well-characterized reference fields and improving the positioning of the sensors on the Hall magnetometer holder. Additionally, the fiducials on the sensors can be used to access the actual sensor positions and orientations optically and compensate for sensor tilting or position deviations by varying the quadrature weights. It is equally important to characterize and, if necessary, compensate for sensor behavior over time. Aging of the sensors, thermal deformations, and mechanical creep would otherwise introduce systematic errors and reduce long-term stability. A thorough investigation of long-term stability is therefore essential for the characterization of a metrological instrument.

Another important step will be the quantification of potential truncation errors when the measured field cannot be accurately represented by a sixth-degree polynomial. This allows fields to be measured without having to know their spatial complexity in advance. For direct verification, additional sensors can be placed within the sphere. Our current sampling rate of 10 Hz does not yet reach hardware limitations, suggesting that an increase by a factor of ten is feasible. Furthermore, the presented methodology is not tied to a specific sensor type. Depending on the requirements of a given application, different magnetometer technologies can be employed to optimize the trade-off between resolution, bandwidth, and dynamic range. For example, the integration of small receiver coils, which are fed via multiplexers to a suitable analogue-to-digital converter and digitized, is a promising approach for AC field measurements. Another interesting direction is extending this

This article has been accepted for publication in IEEE Sensors Journal. This is the author's version which has not been fully edited and
content may change prior to final publication. Citation information: DOI 10.1109/JSEN.2025.3629803

technique to ellipsoidal regions, using ellipsoidal harmonics as the field expansion basis [25], [44]. Since magnetic fields are often generated and analyzed in non-spherical regions, an ellipsoidal approach could better adapt to the actual measurement volume. For instance, tomographic imaging systems typically operate in cylindrical regions, where an ellipsoidal measurement device could provide improved spatial coverage and more accurate field characterization.

DECLARATIONS

Conflict of Interest

The authors declare no competing interests.

REFERENCES

[1] P. C. Lauterbur, "Image formation by induced local interactions. Examples employing nuclear magnetic resonance. 1973." *Clinical orthopaedics and related research*, no. 244, pp. 3–6, Jul. 1989, place: United States.

[2] B. Gleich and J. Weizenecker, "Tomographic imaging using the nonlinear response of magnetic particles," *Nature*, vol. 435, no. 7046, pp. 1214–1217, Jun. 2005. [Online]. Available: http://www.nature.com/articles/nature03808

[3] A. Mukhatov, T. Le, T. T. Pham, and T. D. Do, "A comprehensive review on magnetic imaging techniques for biomedical applications," *Nano Select*, vol. 4, no. 3, pp. 213–230, Mar. 2023. [Online]. Available: https://onlinelibrary.wiley.com/doi/10.1002/nano.202200219

[4] B. E. Dietrich, D. O. Brunner, B. J. Wilm, C. Barmet, S. Gross, L. Kasper, M. Haeberlin, T. Schmid, S. J. Vannesjo, and K. P. Pruessmann, "A field camera for MR sequence monitoring and system analysis," *Magnetic Resonance in Medicine*, vol. 75, no. 4, pp. 1831–1840, Apr. 2016. [Online]. Available: https://onlinelibrary.wiley.com/doi/10.1002/mrm.25770

[5] T. Knopp, N. Gdaniec, and M. Möddel, "Magnetic particle imaging: from proof of principle to preclinical applications," *Physics in Medicine & Biology*, vol. 62, no. 14, p. R124, Jun. 2017, publisher: IOP Publishing. [Online]. Available: https://iopscience.iop.org/article/10.1088/1361-6560/aa6c99/meta

[6] M. Boberg, T. Knopp, and M. Möddel, "Unique compact representation of magnetic fields using truncated solid harmonic expansions," *Nature Communications Physics*, 2025, accepted for publication.

[7] N. Akai and K. Ozaki, "3D magnetic field mapping in large-scale indoor environment using measurement robot and Gaussian processes," in *2017 International Conference on Indoor Positioning and Indoor Navigation (IPIN)*. Sapporo: IEEE, Sep. 2017, pp. 1–7. [Online]. Available: http://ieeexplore.ieee.org/document/8115960/

[8] S. Noguchi, "Formulation of the spherical harmonic coefficients of the entire magnetic field components generated by magnetic moment and current for shimming," *Journal of Applied Physics*, vol. 115, no. 16, p. 163908, 04 2014. [Online]. Available: https://doi.org/10.1063/1.4872244

[9] C. Eccles, S. Crozier, M. Westphal, and D. Doddrell, "Temporal spherical-harmonic expansion and compensation of eddy-current fields produced by gradient pulses," *Journal of Magnetic Resonance, Series A*, vol. 103, no. 2, pp. 135–141, 1993. [Online]. Available: https://www.sciencedirect.com/science/article/pii/S1064185883711447

[10] G. Bringout and T. M. Buzug, "A robust and compact representation for magnetic fields in magnetic particle imaging," *Biomed Tech*, vol. 59, pp. 978–1, 2014.

[11] C. Barmet, N. D. Zanche, and K. P. Pruessmann, "Spatiotemporal magnetic field monitoring for MR," *Magnetic Resonance in Medicine*, vol. 60, no. 1, pp. 187–197, Jul. 2008. [Online]. Available: https://onlinelibrary.wiley.com/doi/10.1002/mrm.21603

[12] A. B. Suksmono, D. Danudirdjo, A. D. Setiawan, D. Rahmawati, and R. P. Prastio, "A Magnetic Field Camera for Real-Time Subsurface Imaging Applications," *Applied Sciences*, vol. 11, no. 8, p. 3302, Apr. 2021. [Online]. Available: https://www.mdpi.com/2076-3417/11/8/3302

[13] C. H. L. Beentjes, "Quadrature on a spherical surface," 2016. [Online]. Available: https://api.semanticscholar.org/CorpusID:19681887

[14] V. Schlageter, P.-A. Besse, R. Popovic, and P. Kucera, "Tracking system with five degrees of freedom using a 2d-array of hall sensors and a permanent magnet," *Sensors and Actuators A: Physical*, vol. 92, no. 1, pp. 37–42, 2001, selected Papers for Eurosensors XIV. [Online]. Available: https://www.sciencedirect.com/science/article/pii/S0924424701005374

[15] C. Vergne, J. Inácio, T. Quirin, D. Sargent, M. Madec, and J. Pascal, "Tracking of a magnetically navigated millirobot with a magnetic-field camera," *IEEE Sensors Journal*, vol. 24, no. 6, pp. 7336–7344, 2024.

[16] H. Nicolas, T. Quirin, and J. Pascal, "Fpga-based magnetic field camera for dynamic magnetic field mapping," *IEEE Sensors Letters*, vol. 8, no. 5, pp. 1–4, 2024.

[17] Y. Kim and X. Zhao, "Magnetic Soft Materials and Robots," *Chemical Reviews*, vol. 122, no. 5, pp. 5317–5364, Mar. 2022, publisher: American Chemical Society (ACS). [Online]. Available: https://pubs.acs.org/doi/10.1021/acs.chemrev.1c00481

[18] D. Son, X. Dong, and M. Sitti, "A Simultaneous Calibration Method for Magnetic Robot Localization and Actuation Systems," *IEEE Transactions on Robotics*, vol. 35, no. 2, pp. 343–352, Apr. 2019. [Online]. Available: https://ieeexplore.ieee.org/document/8594561/

[19] C. Hu, M. Q. Meng, and M. Mandal, "Efficient magnetic localization and orientation technique for capsule endoscopy," in *2005 IEEE/RSJ International Conference on Intelligent Robots and Systems*, 2005, pp. 628–633.

[20] C. Hu, M. Q.-h. Meng, and M. Mandal, "The calibration of 3-axis magnetic sensor array system for tracking wireless capsule endoscope," in *2006 IEEE/RSJ International Conference on Intelligent Robots and Systems*, 2006, pp. 162–167.

[21] M. Turan, Y. Almalioglu, H. B. Gilbert, F. Mahmood, N. J. Durr, H. Araujo, A. E. Sarı, A. Ajay, and M. Sitti, "Learning to navigate endoscopic capsule robots," *IEEE Robotics and Automation Letters*, vol. 4, no. 3, pp. 3075–3082, 2019.

[22] Metrolab. (2024, Dec.) MFC2046 — Metrolab. [Online; accessed December 6, 2024]. [Online]. Available: https://www.metrolab.com/products/products-mfc2046-magnetic-field-camera/

[23] F. Foerger, M. Boberg, J. Faltinath, T. Knopp, and M. Möddel, "Design and optimization of a magnetic field generator for magnetic particle imaging with soft magnetic materials," *Advanced Intelligent Systems*, vol. 6, no. 11, p. 2400017, 2024. [Online]. Available: https://onlinelibrary.wiley.com/doi/abs/10.1002/aisy.202400017

[24] N. Hadjigeorgiou, K. Asimakopoulos, K. Papafotis, and P. P. Sotiriadis, "Vector magnetic field sensors: Operating principles, calibration, and applications," *IEEE Sensors Journal*, vol. 21, no. 11, pp. 12 531–12 544, 2021.

[25] K. Scheffler, L. Meyn, F. Foerger, M. Boberg, M. Möddel, and T. Knopp, "Efficient measurement and representation of magnetic fields in tomographic imaging using ellipsoidal harmonics." *Nature Communications Physics*, 2025, accepted for publication.

[26] A. Weber, *Behandlung von Imperfektionen Bei Magnetic Particle Imaging Mit Hilfe Mathematischer Methoden*. Infinite Science Publishing, 2016.

[27] F. Foerger, N. Hackelberg, M. Boberg, J.-P. Scheel, F. Thieben, L. Mirzojan, F. Mohn, M. Möddel, M. Graeser, and T. Knopp, "Flexible Selection Field Generation using Iron Core Coil Arrays," *International Journal on Magnetic Particle Imaging IJMPI*, p. Vol 9 No 1 Suppl 1 (2023), Mar. 2023, publisher: International Journal on Magnetic Particle Imaging IJMPI. [Online]. Available: https://journal.iwmpi.org/index.php/iwmpi/article/view/624

[28] *TMAG5273 Low-Power Linear 3D Hall-Effect Sensor With I2C Interface*, Texas Instruments, 7 2024.

[29] S. D. Axen, M. Baran, R. Bergmann, and K. Rzecki. (2021) Manifolds.jl: An extensible julia framework for data analysis on manifolds.

[30] R. Bergmann, "Manopt.jl: Optimization on manifolds in Julia," *Journal of Open Source Software*, vol. 7, no. 70, p. 3866, 2022.

[31] J. Bezanson, A. Edelman, S. Karpinski, and V. B. Shah, "Julia: A fresh approach to numerical computing," *SIAM Review*, vol. 59, no. 1, pp. 65–98, 2017. [Online]. Available: https://epubs.siam.org/doi/10.1137/141000671

[32] F. Foerger, P. Suskin, M. Boberg, J. Faltinath, T. Knopp, and M. Möddel, "Uncertainties of a spherical magnetic field camera," 2025. [Online]. Available: https://arxiv.org/abs/2506.17359

[33] F. Thieben, F. Foerger, F. Mohn, N. Hackelberg, M. Boberg, J.-P. Scheel, M. Möddel, M. Graeser, and T. Knopp, "System characterization of a human-sized 3D real-time magnetic particle imaging scanner for cerebral applications," *Communications Engineering*, vol. 3, no. 1, p. 47,

This article has been accepted for publication in IEEE Sensors Journal. This is the author's version which has not been fully edited and content may change prior to final publication. Citation information: DOI 10.1109/JSEN.2025.3629803

Mar. 2024. [Online]. Available: https://www.nature.com/articles/s44172-024-00192-6

[34] T. Knopp, S. Biederer, T. F. Sattel, J. Rahmer, J. Weizenecker, B. Gleich, J. Borgert, and T. M. Buzug, "2d model-based reconstruction for magnetic particle imaging," *Medical Physics*, vol. 37, no. 2, pp. 485–491, 2010. [Online]. Available: https://aapm.onlinelibrary.wiley.com/doi/abs/10.1118/1.3271258

[35] F. Thieben, H. Albers, F. Mohn, F. Foerger, M. Boberg, K. Scheffler, M. Möddel, T. Kluth, and T. Knopp, "Experimental Parameter Calibration of the Scanner Model for Model-Based MPI," *International Journal on Magnetic Particle Imaging IJMPI*, vol. 10, no. 1 Suppl 1, Mar. 2024, publisher: International Journal on Magnetic Particle Imaging IJMPI. [Online]. Available: https://www.journal.iwmpi.org/index.php/iwmpi/article/view/722

[36] K. Wachowicz, "Evaluation of active and passive shimming in magnetic resonance imaging," *Research and Reports in Nuclear Medicine*, p. 1, Oct. 2014. [Online]. Available: http://www.dovepress.com/evaluation-of-active-and-passive-shimming-in-magnetic-resonance-imagin-peer-reviewed-article-RRNM

[37] Z. Yang and L. Zhang, "Magnetic Actuation Systems for Miniature Robots: A Review," *Advanced Intelligent Systems*, vol. 2, no. 9, p. 2000082, Sep. 2020. [Online]. Available: https://onlinelibrary.wiley.com/doi/10.1002/aisy.202000082

[38] V. N. Kharitonov, Z. Z. Namsaraev, R. V. Brizitskii, A. S. Samardak, and A. V. Ognev, "Precise 6-dof motion tracking of fine motor skills of fingers based on wearable magnetic induction sensors," *IEEE Sensors Journal*, vol. 24, no. 7, pp. 11 295–11 305, 2024.

[39] Y. Ma, Z.-H. Mao, W. Jia, C. Li, J. Yang, and M. Sun, "Magnetic hand tracking for human-computer interface," *IEEE Transactions on Magnetics*, vol. 47, no. 5, pp. 970–973, 2011.

[40] T. Lisini Baldi, M. Mohammadi, S. Scheggi, and D. Prattichizzo, "Using inertial and magnetic sensors for hand tracking and rendering in wearable haptics," in *2015 IEEE World Haptics Conference (WHC)*, 2015, pp. 381–387.

[41] H.-M. Shen, "Full-pose magnetic estimation based on a two-stage algorithm for remote hand rehabilitation training," in *Intelligent Robotics and Applications*, Y. Huang, H. Wu, H. Liu, and Z. Yin, Eds. Cham: Springer International Publishing, 2017, pp. 428–437.

[42] L. Ruan, J. Wen, Y. Wang, X. Zhao, F. Li, Y. Zhang, C. Liu, W. Tao, H. Liang, X. Zhang, Y. Zhou, C. Tang, X. Zhong, S. He, and W. Yang, "Sensors and actuators based on magnetic materials for haptic interfaces," *J. Mater. Chem. C*, vol. 13, pp. 16 837–16 862, 2025. [Online]. Available: http://dx.doi.org/10.1039/D5TC00912J

[43] L. Rossi and L. Bottura, "Superconducting magnets for particle accelerators," *Reviews of Accelerator Science and Technology*, vol. 05, pp. 51–89, 2012. [Online]. Available: https://doi.org/10.1142/S1793626812300034

[44] K. Scheffler, L. Meyn, F. Foerger, M. Boberg, M. Martin, and T. Knopp, "Ellipsoidal Harmonic Expansions for Efficient Approximation of Magnetic Fields in Medical Imaging," *International Journal on Magnetic Particle Imaging IJMPI*, vol. 10, no. 1 Suppl 1, Mar. 2024, publisher: International Journal on Magnetic Particle Imaging IJMPI. [Online]. Available: https://www.journal.iwmpi.org/index.php/iwmpi/article/view/725

Fynn Foerger received his B.Sc. and M.Sc. degree in physics from the University of Hamburg, Germany, in 2016 and 2018, respectively.

Currently, he is working as a research assistant at the University Medical Center Hamburg-Eppendorf, Germany and is pursuing the PhD degree at the Hamburg University of Technology, Germany. His current research interests include medical imaging, magnetic field generation and characterization, as well as sensor design and conceptualization.

Marija Boberg is currently pursuing her Ph.D. at the Hamburg University of Technology in Germany, conducting research at a joint institute affiliated with the Hamburg University of Technology and the University Medical Center Hamburg-Eppendorf. She received her Bachelor of Science and Master of Science degrees in Mathematics from the University of Paderborn, Germany. Her current research focuses on magnetic particle imaging, with particular emphasis on the characterization of magnetic fields and image reconstruction.

Niklas Hackelberg received the B.Sc. and M.Sc. degrees in computer science from Hamburg University of Technology (TUHH), Germany, in 2018 and 2021, respectively. He is currently pursuing the Ph.D. degree with the Institute for Biomedical Imaging, University Medical Center Hamburg-Eppendorf, and TUHH. In 2025, he joined the Fraunhofer Research Institution for Individualized and Cell-Based Medical Engineering IMTE in Lübeck, Germany, while continuing his doctoral studies at TUHH. His research interests focus on parallel computing in medical image reconstruction and imaging system instrumentation.

Philip Heinisch received an M. Sc. degree in physics from Technische Universität Braunschweig, Braunschweig, Germany in 2016 followed by his Ph.D. in 2019. He is currently Managing Director of PHYMAG GmbH, Braunschweig, Germany. He focuses on hardware development, embedded systems and sensor design.

Katharina Ostaszewski received the B.Sc. degree in Computer Science from Technische Universität Braunschweig, Braunschweig, Germany, in 2019, and the M.Sc. and Ph.D. degrees in Physics from the same university in 2017 and 2021, respectively. She is currently the Managing Director of PHYMAG GmbH, Braunschweig, Germany. Her current professional focus includes embedded development and magnetic field sensor technology.

Jonas Faltinath received the B.Sc. and M.Sc. degrees in physics from the University of Hamburg, Hamburg, Germany, in 2019 and 2022, respectively. He is pursuing the Ph.D. degree with Hamburg University of Technology, Hamburg.

From 2022 to 2023, he worked as a Researcher at the Ecole Polytechnique Fédérale de Lausanne (EPFL), Lausanne, Switzerland. Currently, he is working as a Research Assistant with the University Medical Center Hamburg-Eppendorf, Hamburg. His current research interests include magneto-mechanical resonators, sensor conceptualization and development, and medical imaging techniques.

This article has been accepted for publication in IEEE Sensors Journal. This is the author's version which has not been fully edited and content may change prior to final publication. Citation information: DOI 10.1109/JSEN.2025.3629803

Philip Suskin received the B.Sc. degree in Computer Engineering and the M.Sc. degree in Computer Science at the Hamburg University of Technology, Hamburg, Germany, in 2022 and 2025, respectively. He is pursuing the Ph.D. degree with Hamburg University of Technology, Hamburg. He is currently working as a Research Assistant with the University Medical Center Hamburg-Eppendorf, Hamburg. His current research interests include medical imaging, magnetic field prediction and power-efficient control, as well as image reconstruction and algorithmic quality estimation.

Florian Thieben received the B.Sc. and M.Sc. degrees in electrical engineering from Hamburg University of Technology (TUHH), Germany, in 2015 and 2017, respectively. He is currently pursuing the Ph.D. degree with the Institute for Biomedical Imaging, University Medical Center Hamburg-Eppendorf, and TUHH. In 2025, he joined the Department of Diagnostics at the Fraunhofer Research Institution for Individualized and Cell-Based Medical Engineering IMTE in Lübeck, Germany, while continuing his doctoral studies at TUHH. His research interests include hardware development for upscaling magnetic particle imaging (MPI) systems for human applications and MPI receive chain calibration.

Fabian Mohn received the master's degree in electrical engineering from Hamburg University of Technology in cooperation with the Philips Research Laboratories, Hamburg, Germany, in 2018, and the Ph.D. degree from Hamburg University of Technology, in 2024. He joined the research group of Tobias Knopp for Biomedical Imaging, University Medical Center Hamburg-Eppendorf, Hamburg, and Hamburg University of Technology, in 2020. His research interests include medical imaging and inductive sensors.

Paul Jürß received the bachelor's degree in computer science and engineering from Hamburg University of Technology in 2020 and the master's degree in industrial mathematics from the University of Hamburg in 2022.

Since 2022, he is working as a Ph.D. candidate in the Biomedical Imaging research group led by Tobias Knopp at the University Medical Center Hamburg-Eppendorf and the Hamburg University of Technology. His research interests include inverse problems, artifact reduction, motion estimation, and machine learning.

Martin Möddel received his physics Diploma in 2011 from the Leipzig University, Germany and his PhD in 2014 from the University of Siegen, Germany.

He is currently working as a postdoctoral researcher at the Institute of Biomedical Imaging which is jointly affiliated with the University Medical Center Hamburg-Eppendorf and the Hamburg University of Technology in Germany. His current research interests include inverse problems, particularly image reconstruction and artifact reduction, magnetic field generation and characterization, and signal processing, with applications in various areas of medical engineering.

Tobias Knopp received his Diplom degree in computer science in 2007 and his PhD in 2010, both from the University of Lübeck, Germany.

He is currently a professor of Biomedical Imaging with a joint appointment at the University Medical Center Hamburg-Eppendorf and the Hamburg University of Technology, Germany. In addition, he heads the Department of Diagnostics at the Fraunhofer Research Institution for Individualized and Cell-Based Medical Engineering IMTE in Lübeck, Germany. His current research interests include signal processing, inverse problems, tracking, sensing, and image reconstruction, with applications across various areas of medical engineering.